Nano Research

Open Access

Research Article

Synergistic design of embedded heterojunctions and hollow architecture for superior HER in acidic and alkaline electrolytes

Dian Yang[1], Can Chen[1], Huanhuan Zhang[1], Junjie Gong[1], LiLi Zhang[1] ✉, Lin Gu[2], Shijie Shen[1,3] ✉, and Wenwu Zhong[3] ✉

[1] *Zhejiang Key Laboratory for Island Green Energy and New Materials, Taizhou University, Jiaojiang 318000, China*
[2] *Beijing National Center for Electron Microscopy and Laboratory of Advanced Materials, Department of Materials Science and Engineering, Tsinghua University, Beijing 100084, China*
[3] *Zhejiang Key Laboratory of Functional ionic membrane Materials and Technology for Hydrogen Production, Shaoxing University, Shaoxing 312000, China*

Cite this article: *Nano Research*, **2026**, *19*, 94908616. https://doi.org/10.26599/NR.2026.94908616

ABSTRACT: Ruthenium phosphide electrocatalysts for the hydrogen evolution reaction (HER) still face challenges such as insufficient active site utilization and limited durability. This work addresses these challenges via a synergistic strategy that integrates heterojunction engineering with a hollow confinement structure, resulting in RuP_2-Ni_2P nanoparticles embedded within N,P-codoped hollow carbon spheres (RuP_2-Ni_2P/NPC). The interfacial coupling between RuP_2 and Ni_2P optimizes the electronic structure toward a near-ideal hydrogen adsorption energy, while the unique embedded architecture ensures abundant accessible active sites and exceptional structural robustness. As a result, the RuP_2-Ni_2P/NPC catalyst exhibits superior HER performance across a wide pH range, achieving ultralow overpotentials of 3 mV in 1 M KOH and 17.3 mV in 0.5 M H_2SO_4 at 10 mA·cm^{-2}, ranking among the best of reported RuP_2-based catalysts. It also demonstrates excellent long-term durability in both alkaline and acidic electrolytes. This work provides a feasible design strategy toward efficient and robust electrocatalysts for hydrogen production.

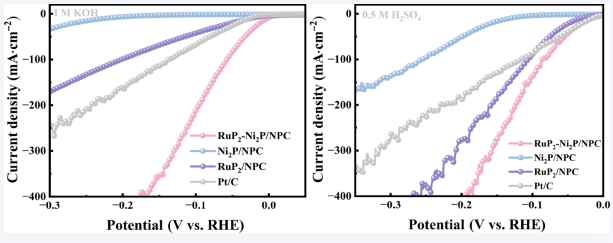

KEYWORDS: hydrogen evolution reaction (HER), ruthenium phosphide, heterojunction, hollow carbon spheres, electrocatalyst

1 Introduction

The development of efficient, stable, and cost-effective electrocatalysts is crucial for advancing the industrialization of water-splitting hydrogen production [1–4]. Currently, platinum (Pt)-based catalysts are considered the benchmark due to their exceptional activity. However, their high cost and limited reserves pose significant bottlenecks for large-scale applications [5]. In this context, the search for non-precious or low-platinum-group-metal alternatives with "Pt-like" performance has become a central research focus [6–10]. Ruthenium (Ru) has attracted considerable attention owing to its moderate price and hydrogen binding strength analogous to that of Pt [11]. In particular, ruthenium phosphide (RuP_2) has emerged as a promising candidate. The incorporation of phosphorus atoms effectively modulates the electronic state of Ru, often yielding a near-thermoneutral hydrogen adsorption free energy [12, 13]. This property enables excellent intrinsic hydrogen evolution reaction (HER) activity across a wide pH range, establishing RuP_2 as a highly promising Pt-alternative candidate [14–18].

To fully exploit the catalytic potential of RuP_2, researchers have developed sophisticated design strategies, primarily centered on electronic structure modulation and nanostructure engineering [19–22]. For electronic structure optimization, constructing heterointerfaces is a mainstream approach. For instance, creating intimate contact between RuP_2 and other metal phosphides (e.g., CoP, WP) [23, 24] or between different ruthenium phosphide phases (e.g., RuP) [25] can induce interfacial charge transfer due to work function differences. This charge transfer optimizes the adsorption strength of reaction intermediates on active sites. Furthermore, doping with heteroatoms (e.g., W, S) [20, 26] has been shown to fine-tune the d-band center of Ru, consequently improving catalytic kinetics. Regarding nanostructure engineering,

Received: February 5, 2026; **Revised:** March 2, 2026
Accepted: March 3, 2026

✉Address correspondence to LiLi Zhang, zhanglily@tzc.edu.cn; Shijie Shen, shensj@tzc.edu.cn; Wenwu Zhong, zhongww@tzc.edu.cn

a common strategy involves loading RuP_2 nanoparticles or clusters onto high-surface-area, conductive carbon-based supports (e.g., N/P co-doped carbon) [27, 28]. This aims to prevent particle aggregation, increase active site exposure, and facilitate electron transport. However, these strategies still face two major common challenges. On one hand, complex architectures often lead to insufficient utilization of active sites. This leaves significant room for improvement in the mass activity of the precious metal [29]. On the other hand, it remains difficult to concurrently achieve long-term structural and chemical stability under high current densities [30]. Issues such as dissolution and aggregation of active components, or corrosion of the support, limit their practical application potential.

Here, we propose a synergistic strategy that integrates heterojunction-induced electronic modulation with a hollow-confinement structural design, successfully constructing N,P-codoped hollow carbon sphere-supported RuP_2-Ni_2P nanoparticles (RuP_2-Ni_2P/NPC). This integrated design simultaneously addresses the key challenges mentioned above: the RuP_2-Ni_2P heterointerface effectively optimizes the hydrogen adsorption energy of the active sites through interfacial electron redistribution, while the firm embedding of ultrafine heterojunction nanoparticles into the shell of the hollow carbon spheres ensures maximal exposure of active sites. Moreover, the confinement and protective effects provided by the carbon shell greatly enhance the mechanical stability and durability of the catalyst. As a result, the obtained RuP_2-Ni_2P/NPC exhibits record-low overpotentials and outstanding long-term stability for the hydrogen evolution reaction across both alkaline and acidic media, representing one of the best-performing RuP_2-based catalysts reported to date. This work not only demonstrates a high-performance, cost-effective catalyst but also offers a general design principle for developing robust heterojunction electrocatalysts toward practical hydrogen production.

2 Experimental methods

2.1 Synthesis of NHCSs

Nitrogen-doped hollow carbon spheres (NHCSs) were synthesized via a template-assisted method. Briefly, 24 mL of anhydrous ethanol, 1.0 mL of ammonia solution (28 wt.%), and 80 mL of deionized water were mixed in a beaker under vigorous magnetic stirring. After 10 min, 1 mL of tetraethyl orthosilicate (TEOS) was added dropwise, and the stirring was continued for another 10 min. Subsequently, 8 mL of an aqueous dopamine (DA) solution (100 mg·mL^{-1}) was introduced into the mixture. The reaction was allowed to proceed under continuous stirring for 24 h at room temperature. The resulting solid product was collected by centrifugation, washed three times with deionized water, and dried overnight at 60 °C. The dried powder was ground and then annealed at 800 °C for 4 h under an Ar atmosphere. To remove the SiO_2 template, the carbonized product was dispersed in a 10 wt.% HF aqueous solution and etched for 25 min. Finally, the NHCSs were obtained by filtration, washed thoroughly with deionized water, and dried in air overnight.

2.2 Synthesis of RuP_2-Ni_2P/NPC

The RuP_2-Ni_2P/NPC composite was prepared via an ion adsorption method followed by thermal phosphidation. Typically, 100 mg of the as-prepared NHCSs was ultrasonically dispersed in 20 mL of deionized water. Subsequently, 0.48 mmol of $RuCl_3{\cdot}xH_2O$ and 0.48 mmol of $Ni(NO_3)_2{\cdot}6H_2O$ were added sequentially under magnetic stirring. After stirring for 10 min, the mixture was further treated with ultrasonication for 2 h to ensure homogeneous dispersion of the metal precursors. The mixture was then transferred to an oil bath and heated at 80 °C with stirring at 400 rpm until the solvent was completely evaporated. The resulting solid was further dried overnight in an oven at 60 °C.

The phosphidation process was carried out in a tube furnace under an Ar flow. The dried powder was placed in a ceramic boat, while 2 g of $NaH_2PO_2{\cdot}H_2O$ was positioned upstream as the phosphorus source. The temperature was raised to 800 °C at a ramping rate of 3 °C·min^{-1}, held for 1 h, and then allowed to cool to room temperature naturally. The final product, denoted as RuP_2-Ni_2P/NPC, was collected.

To investigate the effect of precursor loading, samples were synthesized using total metal amounts of 0.24, 0.48, and 0.72 mmol while maintaining a Ru:Ni molar ratio of 1:1. To study the influence of the metal ratio, samples with Ru:Ni molar ratios of 1:1, 2:1, and 1:2 were prepared, keeping the total metal amount constant at 0.48 mmol.

2.3 Synthesis of RuP_2/NPC and Ni_2P/NPC

For comparison, reference samples containing only a single metal phosphide were prepared following a similar procedure. The RuP_2/NPC sample was synthesized using only 0.48 mmol of $RuCl_3{\cdot}xH_2O$ as the metal precursor. Similarly, the Ni_2P/NPC sample was prepared using only 0.48 mmol of $Ni(NO_3)_2{\cdot}6H_2O$. All other steps, including the adsorption, drying, and phosphidation conditions, were identical to those described for the RuP_2-Ni_2P/NPC composite.

2.4 Materials characterization

The crystal structures of the prepared samples were investigated by X-ray diffraction (XRD) using a Bruker D8 Advance diffractometer equipped with Cu Kα radiation (λ = 0.15406 nm). Morphological and microstructural analyses were conducted using a Hitachi S4800 field-emission scanning electron microscope (SEM) and a Thermo Scientific Talos F200i transmission electron microscope (TEM). Elemental distribution within the samples was examined through energy-dispersive X-ray spectroscopy (EDS) mapping performed on the TEM system. The chemical composition and metal loading were determined by inductively coupled plasma optical emission spectroscopy (ICP-OES) on an Agilent 5110 instrument. Surface chemical states and elemental analysis were probed by X-ray photoelectron spectroscopy (XPS) using a Thermo Scientific K-Alpha spectrometer with an Al Kα X-ray source.

2.5 Electrochemical measurements

All electrochemical measurements were performed using a CHI 760e electrochemical workstation with a standard three-electrode configuration. For tests in a 1.0 M KOH aqueous electrolyte, a Hg/HgO electrode and a graphite rod were employed as the reference and counter electrodes, respectively. For tests in a 0.5 M H_2SO_4 aqueous electrolyte, an Ag/AgCl electrode served as the reference electrode. A glassy carbon electrode (GCE, 5 mm in diameter) was used as the working electrode for linear sweep voltammetry (LSV), cyclic voltammetry (CV), and electrochemical impedance spectroscopy (EIS) measurements. For stability tests, a carbon paper substrate (0.5 cm × 0.5 cm) was used as the working

electrode to mitigate interference from hydrogen bubble accumulation and to facilitate post-stability characterization.

To prepare the working electrode, a homogeneous ink was formulated by dispersing 5 mg of the catalyst sample in 1 mL of a 3:1 (v/v) ethanol-isopropanol mixture, followed by ultrasonication for 20 min. Then, 50 μL of a 5 wt.% Nafion solution was added, and the mixture was further sonicated for another 20 min. An aliquot of the resulting ink was drop-cast onto the surface of the GCE or carbon paper and dried at room temperature to form a uniform catalyst layer.

LSV curves were recorded at a scan rate of 5 $mV \cdot s^{-1}$. Tafel slopes were derived from the corresponding polarization curves. CV was conducted at various scan rates (20, 30, 40, 50, 60, 70, and 80 $mV \cdot s^{-1}$). EIS measurements were performed at the open-circuit potential over a frequency range from 10^5 to 10^{-1} Hz, and the data are presented in Nyquist plots. Long-term chronopotentiometry (CP) tests were conducted at a constant current density of 100 $mA \cdot cm^{-2}$. All applied potentials were referenced to the reversible hydrogen electrode (RHE) scale using the following conversion equations: $E_{RHE} = E_{Hg/HgO} + 0.059 \times pH + 0.098$ V in 1.0 M KOH, and $E_{RHE} = E_{Ag/AgCl} + 0.059 \times pH + 0.197$ V in 0.5 M H_2SO_4.

2.6 *In situ* Raman spectroscopy

In situ Raman spectroscopic measurements were conducted using a Horiba Jobin Yvon HR Evolution system equipped with a 532 nm laser. The experiment was performed in a custom-designed electrochemical cell integrated with a Raman microscope. The spectra were collected through a 50× microscope objective during the application of controlled electrochemical potentials.

2.7 Density functional theory (DFT) calculations

All spin-polarized DFT calculations were carried out using the Vienna *ab initio* simulation package (VASP) [31]. The projector augmented-wave (PAW) method [32] was employed to describe the core–electron interactions, and the generalized gradient approximation (GGA) with the Perdew–Burke–Ernzerhof (PBE) functional [33] was adopted for the exchange–correlation energy. van der Waals interactions were accounted for using the DFT-D3 method with zero damping [34]. A plane-wave energy cutoff of 450 eV was applied, and structural relaxations were performed until the residual forces on all atoms were below 0.02 $eV \cdot Å^{-1}$. The energy convergence criterion was set to 1×10^{-5} eV. A vacuum spacing of at least 15 Å was introduced normal to the surface to avoid periodic interactions. A 3 × 3 × 1 Monkhorst–Pack *k*-point mesh was used for geometry optimization and electronic structure analysis. To better describe the localized d electrons of Ni and Ru, a Hubbard *U* correction was applied with effective *U* values of 3.40 eV for Ni and 2.40 eV for Ru [35].

3 Results and discussion

3.1 Synthesis, structure, and composition of RuP_2-Ni_2P/NPC

In this work, RuP_2-Ni_2P heterojunction material supported on N,P-codoped hollow carbon spheres (RuP_2-Ni_2P/NPC) was successfully synthesized via a template method combined with subsequent ion adsorption and phosphidation. First, using SiO_2 as a hard template, a core–shell structure of N-doped carbon coated on SiO_2 was prepared through dopamine polymerization and subsequent high-temperature carbonization. Then, the SiO_2 core was etched away using an HF solution to obtain nitrogen-doped hollow carbon spheres (NHCSs) as the precursor. Finally, Ru^{3+} and Ni^{2+} precursors were loaded via an impregnation method, followed by high-temperature phosphidation to yield the final product. The phosphidation process not only formed the metal phosphides but also achieved phosphorus doping into the carbon framework.

The crystal structure of the NHCSs carrier was confirmed by XRD. As shown in Fig. S1 in the Electronic Supplementary Material (ESM), the XRD pattern exhibits two broad diffraction peaks at approximately 22.4° and 43.6°. These peaks correspond to the (002) and (101) planes of graphitic carbon, respectively, confirming the successful formation of an amorphous carbon matrix. SEM and TEM images (Fig. S2 in the ESM) reveal that the obtained NHCSs are hollow spheres with a diameter of about 200 nm, featuring a smooth surface and uniform dispersion.

The morphology and microstructure of the RuP_2-Ni_2P/NPC composite were further characterized. Low-magnification SEM and TEM images (Figs. 1(a) and 1(b)) show that the composite largely retains the hollow spherical morphology. However, a large number of tiny nanoparticles are embedded on the surface of the spheres. High-resolution TEM (HRTEM) imaging (Fig. 1(c)) reveals the fine structure of these nanoparticles. Clear lattice fringes with spacings of 0.23 and 0.22 nm are observed, matching the (111) crystal planes of RuP_2 (PDF #34-0333) and Ni_2P (PDF #03-0953), respectively. This provides direct evidence for the successful construction of RuP_2-Ni_2P heterojunction nanoparticles. Furthermore, TEM-EDS mapping (Fig. 1(d)) shows a uniform distribution of C, N, Ru, Ni, and P elements throughout the hollow sphere carrier, indicating the high dispersion of metal phosphide nanoparticles on the NPC surface.

XRD analysis provides further crystallographic evidence for heterojunction formation. As shown in Fig. 1(e), the diffraction pattern of RuP_2-Ni_2P/NPC shows peaks at approximately 40.2°, 44.2°, and 47.2°, which can be assigned to the characteristic peaks of RuP_2 and Ni_2P, respectively. No other impurity phases are detected, which is consistent with the HRTEM results and confirms the existence of the RuP_2-Ni_2P heterostructure.

The pore structure of the materials was investigated using N_2 adsorption–desorption measurements. As shown in Fig. 1(f), both NHCSs and RuP_2-Ni_2P/NPC exhibit typical type IV isotherms, indicating the presence of abundant mesoporous structures. Calculated using the BET model, the specific surface area of NHCSs is as high as 1207.2 $m^2 \cdot g^{-1}$. After loading RuP_2-Ni_2P, the specific surface area of the composite decreases to 271.4 $m^2 \cdot g^{-1}$. This decrease can be attributed to the partial embedding or occupation of the carbon sphere surface pores by the metal phosphide nanoparticles. Nevertheless, RuP_2-Ni_2P/NPC retains a relatively large specific surface area, which helps expose more active sites and promote mass transport. The pore size distribution curves (inset of Fig. 1(f)) further confirm that both materials are primarily mesoporous.

For comparison, single-component RuP_2/NPC and Ni_2P/NPC samples were also synthesized. Their XRD and TEM characterization results (Figs. S3–S5 in the ESM) confirm the successful preparation of the single metal phosphides. The precise metal loadings in each sample were determined by ICP-OES (Table S1 in the ESM). In RuP_2-Ni_2P/NPC, the mass fractions of Ru and Ni are 6.11% and 7.02%, respectively, corresponding to a Ru/Ni

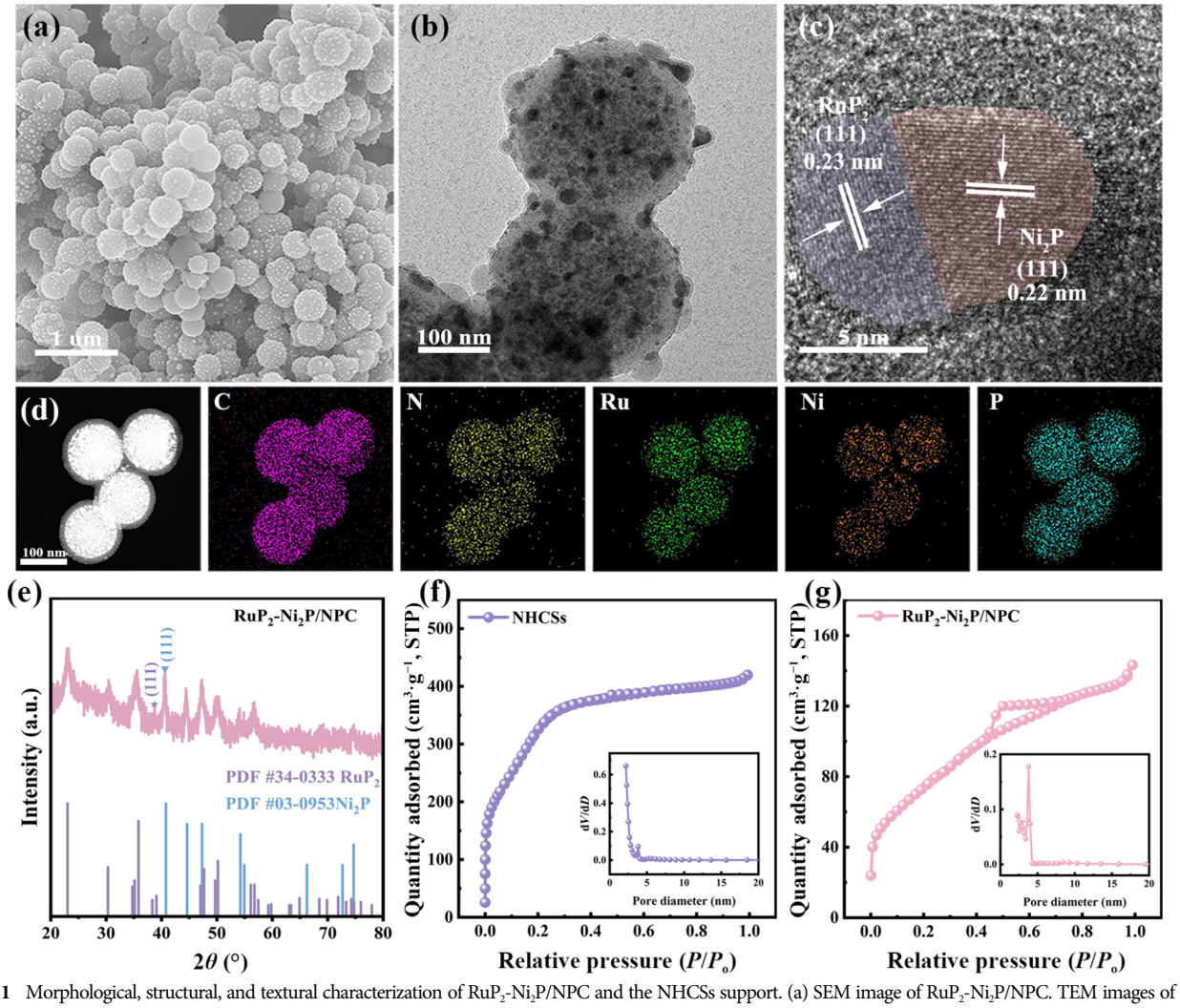

Figure 1 Morphological, structural, and textural characterization of RuP_2-Ni_2P/NPC and the NHCSs support. (a) SEM image of RuP_2-Ni_2P/NPC. TEM images of RuP_2-Ni_2P/NPC at (b) low and (c) high magnifications. (d) TEM image and the corresponding EDS elemental mapping of RuP_2-Ni_2P/NPC. (e) XRD pattern of RuP_2-Ni_2P/NPC. N_2 adsorption–desorption isotherms of (f) NHCSs and (g) RuP_2-Ni_2P/NPC; the insets show the corresponding pore size distribution curves calculated by the BJH method.

molar ratio close to 1:1. The P content is 11.28%, which is higher than the stoichiometric ratio required for forming RuP_2 and Ni_2P, attributable to the successful doping of phosphorus into the carbon skeleton.

To investigate the surface chemical states and electronic interactions between elements, XPS analysis was conducted. The high-resolution Ru 3p spectrum (Fig. 2(a)) reveals a slight but discernible positive shift of 0.05 eV in the binding energy of the Ru $3p_{3/2}$ peak for RuP_2-Ni_2P/NPC compared to RuP_2 /NPC. Conversely, in the Ni 2p spectrum (Fig. 2(b)), the characteristic $Ni^{\delta+}$ peak for RuP_2-Ni_2P/NPC is shifted by 0.66 eV toward lower binding energy relative to that of Ni_2P/NPC. This opposite shift trend in binding energies indicates the formation of an intimate heterointerface between RuP_2 and Ni_2P, inducing interfacial electron transfer from RuP_2 to Ni_2P. In the P 2p spectrum (Fig. 2(c)), peaks at 133.3 and 134.2 eV can be assigned to P–C/N bonds and surface-oxidized P-O bonds, respectively [36]. The former confirms successful phosphorus doping into the carbon carrier [37]. The N 1s spectrum (Fig. 2(d)) can be deconvoluted into two configurations: pyridinic N (398.3 eV) and graphitic N (401.3 eV) [38], which help improve the conductivity of the carbon carrier.

3.2 Evaluation of electrocatalytic hydrogen evolution performance

To optimize the synthesis conditions, the HER performance of the catalysts was first evaluated in 1 M KOH electrolyte. The effects of the total metal precursor amount (M = 0.24, 0.48, and 0.72 mmol) and the Ru/Ni molar ratio (1:1, 1:2, and 2:1) on catalytic activity were systematically investigated (Figs. S6 and S7 in the ESM). The results demonstrate that the RuP_2-Ni_2P/NPC sample prepared with a total metal precursor amount of 0.48 mmol and a Ru:Ni molar ratio of 1:1 exhibits optimal HER activity. This optimal metal loading achieves a balance between sufficient active site availability and the prevention of excessive particle agglomeration. Specifically, a lower metal loading (0.24 mmol) may result in an insufficient number of active sites. In contrast, a higher loading (0.72 mmol) tends to induce nanoparticle agglomeration or blockage of the hollow carbon support pores. This blockage can reduce the accessible surface area and mass transfer efficiency of the catalyst. Consequently, all subsequent detailed performance evaluations and mechanistic analyses were conducted on the catalyst prepared under these optimized conditions.

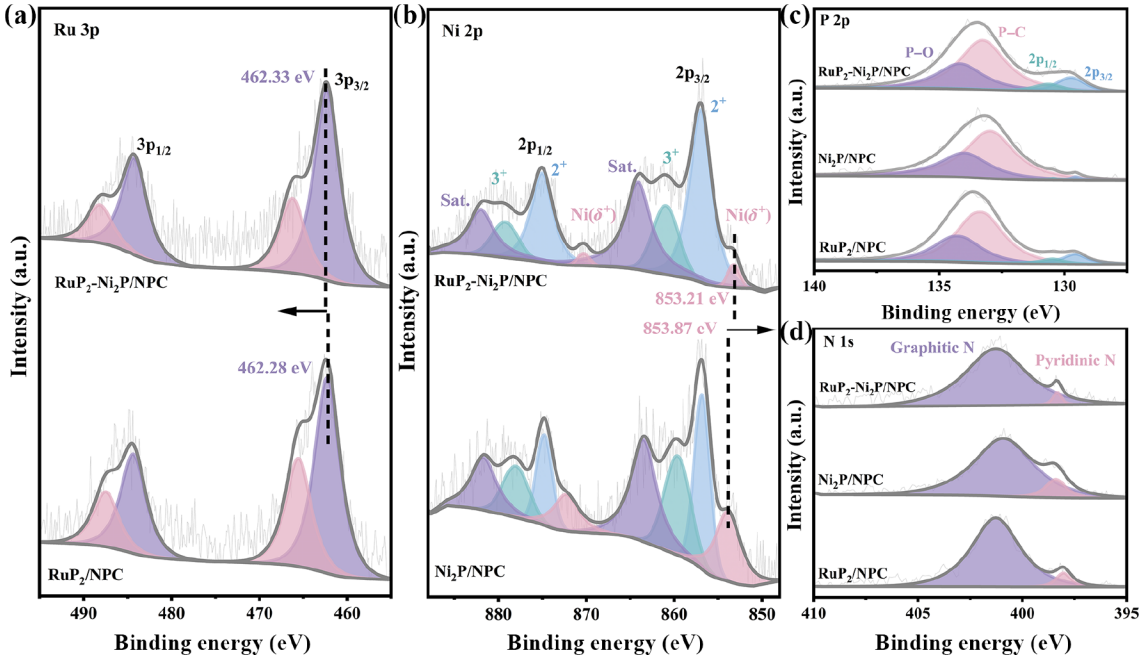

Figure 2 XPS analysis of the chemical states. (a) High-resolution Ru 3p spectra of RuP_2-Ni_2P/NPC and RuP_2/NPC. (b) High-resolution Ni 2p spectra of RuP_2-Ni_2P/NPC and Ni_2P/NPC. (c) P 2p spectra of RuP_2-Ni_2P/NPC, RuP_2/NPC, and Ni_2P/NPC. (d) N 1s spectra of RuP_2-Ni_2P/NPC, RuP_2/NPC, and Ni_2P/NPC.

In 1 M KOH electrolyte, the optimized RuP_2-Ni_2P/NPC demonstrates outstanding catalytic activity. LSV curves (Fig. 3(a)) show that it requires overpotentials (η_{10}) of only 3, 33, and 58 mV to achieve current densities of 10, 50, and 100 mA·cm^{-2}, respectively (Fig. 3(b)). This performance is significantly superior to that of commercial Pt/C (29, 81, and 136 mV), RuP_2/NPC (26, 116, and 202 mV), and Ni_2P/NPC (η_{10} = 225 mV). This enhancement is primarily attributed to the formation of the RuP_2-Ni_2P heterostructure. The corresponding Tafel slope (Fig. 3(c)) shows that RuP_2-Ni_2P/NPC (34.13 mV·dec^{-1}) is lower than that of Pt/C (43.08 mV·dec^{-1}), indicating faster HER kinetics. Compared with recently reported advanced catalysts (Fig. 3(d) and Table S2 in the ESM), RuP_2-Ni_2P/NPC achieves one of the lowest overpotentials among known RuP_2-based materials for alkaline HER.

To evaluate the economic efficiency of the catalyst, the mass activity normalized by precious metal mass was calculated. As shown in Fig. S8 in the ESM, at an overpotential of −100 mV, the Ru mass activity of RuP_2-Ni_2P/NPC (−5.107 A·mg$_{Ru}^{-1}$) is 10.3 times that of the Pt mass activity of Pt/C (−0.493 A·mg$_{Pt}^{-1}$) and 11.3 times that of RuP_2/NPC (−0.449 A·mg$_{Ru}^{-1}$), highlighting its excellent noble metal atom utilization efficiency.

The electrochemical active surface area (ECSA) of the catalysts was evaluated by determining the double-layer capacitance (C_{dl}) from CV curves (Fig. S9 in the ESM). The RuP_2-Ni_2P/NPC electrode exhibits a C_{dl} value of 156.3 mF·cm^{-2}, which is substantially higher than those of Ni_2P/NPC (111.6 mF·cm^{-2}) and RuP_2/NPC (46.4 mF·cm^{-2}). This result indicates that the construction of the RuP_2-Ni_2P heterostructure facilitates the exposure of more electrochemically active sites. EIS shows that it also exhibits the smallest charge transfer resistance (Fig. S10 in the ESM), consistent with its superior kinetic performance. To decouple the contribution of increased surface area from genuine enhancement in intrinsic activity, the LSV curves were normalized by ECSA (Fig. S11 in the ESM). The resulting ECSA-normalized polarization curves reveal that RuP_2-Ni_2P/NPC still delivers the highest current density per unit active surface area, confirming that the formation of the RuP_2-Ni_2P heterojunction intrinsically boosts the catalytic activity at each active site.

Long-term stability is crucial for practical application. At a constant current density of 100 mA·cm^{-2}, RuP_2-Ni_2P/NPC can operate stably in 1 M KOH for 500 h without significant performance degradation (Fig. 3(e)). ICP-OES analysis of the electrolyte after the stability test (Table S3 in the ESM) shows that the dissolution concentrations of Ru, Ni, and P elements are extremely low, demonstrating excellent chemical stability. Furthermore, post-stability characterization by SEM (Fig. S12(a) in the ESM), TEM (Fig. S12(b) in the ESM), and XRD (Fig. S13 in the ESM) reveals no significant changes. Specifically, the hollow sphere structure, the embedded nanoparticle morphology, and the crystalline phases remain intact. This confirms outstanding structural stability.

In 0.5 M H_2SO_4 acidic medium, RuP_2-Ni_2P/NPC also exhibits excellent hydrogen evolution reaction (HER) activity. At a current density of 10 mA·cm^{-2}, this catalyst requires an overpotential of only 17.3 mV, outperforming Pt/C and the single-component counterparts (Figs. 3(f) and 3(g)). Consistent with the observations in alkaline electrolyte, the RuP_2-Ni_2P/NPC sample prepared with a total metal precursor amount of 0.48 mmol and a Ru:Ni molar ratio of 1:1 demonstrates the optimal HER activity under acidic conditions as well (Figs. S14 and S15 in the ESM). The corresponding Tafel slope is 43.59 mV·dec^{-1} (Fig. 3(h)), indicating fast reaction kinetics.

The mass activity of RuP_2-Ni_2P/NPC was further evaluated. At an overpotential of −100 mV, it achieves a mass activity of −3.274 A·mg$_{Ru}^{-1}$, which is five times higher than that of Pt/C (−0.643 A·mg$_{Pt}^{-1}$) (Fig. S16 in the ESM). ECSA measurements, ECSA-normalized LSV curves, and EIS analysis (Figs. S17–S19 in the ESM) collectively confirm that the catalyst can maximize accessible active sites, enhance intrinsic catalytic activity, and accelerate interfacial charge transfer in acidic medium.

Compared with previously reported catalysts (Fig. 3(i) and Table

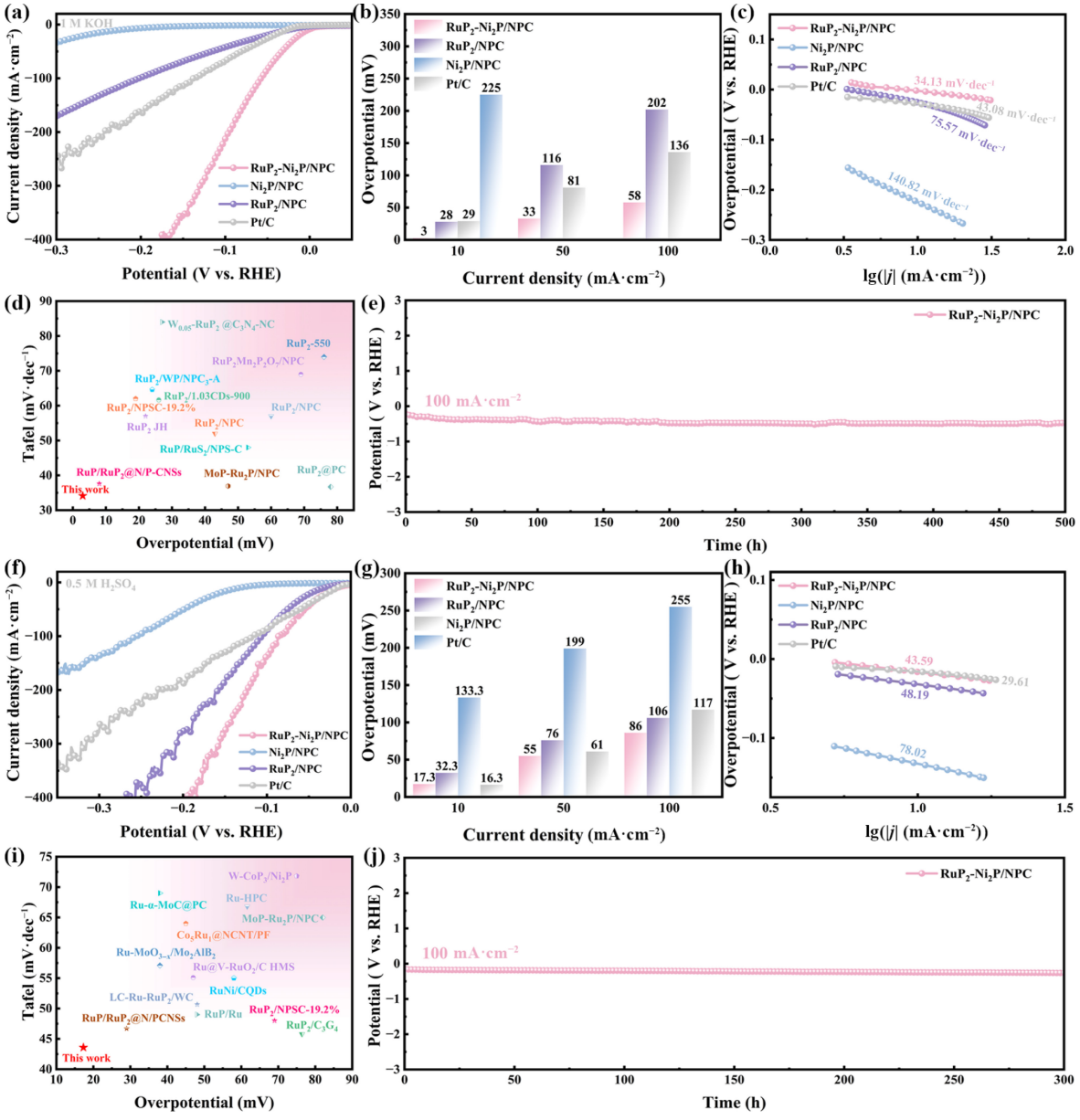

Figure 3 Electrocatalytic HER performance of RuP_2-Ni_2P/NPC in alkaline and acidic electrolytes. (a) Polarization curves in 1 M KOH. (b) Overpotentials required to achieve current densities of 10, 50, and 100 mA·cm^{-2}. (c) Corresponding Tafel slopes. (d) Comparison of overpotential and Tafel slope for RuP_2-Ni_2P/NPC with those of recently reported RuP_2-based catalysts in 1 M KOH. (e) Chronopotentiometry stability test conducted at a constant current density of 100 mA·cm^{-2} for 500 h. Corresponding performance evaluations in 0.5 M H_2SO_4: (f) polarization curves, (g) overpotentials, (h) Tafel slopes, (i) comparison of overpotential for RuP_2-Ni_2P/NPC with those of reported RuP_2-based catalysts in 0.5 M H_2SO_4, and (j) stability test at 100 mA·cm^{-2} for 300 h. The data in (d) and (i) are taken from Refs. [18, 24, 25, 30, 38–56]) (see Tables S2 and S4 in the ESM for detailed comparisons).

S4 in the ESM), RuP_2-Ni_2P/NPC ranks among the top-performing HER electrocatalysts in acidic electrolyte. Furthermore, a 300-hour chronopotentiometry test conducted at a current density of 100 mA·cm^{-2} (Fig. 3(j)), together with ICP-OES analysis of the post-reaction electrolyte (Table S5 in the ESM) and characterization of the catalyst's morphology and phase structure after the stability test (Figs. S20 and S21 in the ESM), collectively demonstrate its excellent long-term operational stability under acidic conditions.

3.3 Reaction mechanism and theoretical calculation analysis

To investigate the origin of activity, *in situ* Raman spectroscopy was first conducted. In both 1 M KOH and 0.5 M H_2SO_4, a distinct vibrational peak at ~ 1809 cm^{-1} is observed when the applied potential reaches −0.02 V (vs. RHE) (Figs. 4(a) and 4(b)) [57]. This peak can be assigned to the stretching vibration of the Ru–H bond, and its signal intensity increases with increasing overpotential. This result directly confirms that Ru sites are the key hydrogen adsorption active centers during the HER process.

To further elucidate the performance enhancement mechanism of the RuP_2-Ni_2P heterostructure at the atomic level, DFT calculations were performed in this work. Based on the HRTEM characterization results (Fig. 1(c)), lattice fringes with spacings of 0.23 and 0.22 nm were clearly observed. These spacings correspond to the (111) planes of Ni_2P and RuP_2, respectively. Accordingly, a

heterojunction model consisting of Ni_2P (111) and RuP_2 (111) was constructed (Fig. 4(c) and Fig. S22 in the ESM). Work function calculations (Figs. 4(d)–4(f)) show that the work function of RuP_2 (4.471 eV) is lower than that of Ni_2P (4.962 eV), with a difference of 0.491 eV. This thermodynamically drives electron transfer from the lower work function RuP_2 to Ni_2P. The charge density difference plot (Fig. S23 in the ESM) quantitatively shows that approximately 0.13 e of charge transfers from the RuP_2 side to the Ni_2P side at the heterojunction interface. This finding is fully consistent with the binding energy shift trend observed by XPS, confirming interfacial charge redistribution.

Density of states (DOS) analysis reveals changes in the electronic structure (Fig. 4(g)). After heterojunction formation, the d-band centers of both Ru and Ni shift towards the Fermi level. According to d-band center theory, this upward shift optimizes the adsorption strength between active sites and reaction intermediates [58]. Specifically for the HER process, under alkaline conditions (Fig. 4(h)), the energy barrier for the water dissociation step on the Ni_2P-RuP_2 heterojunction model (−1.090 eV) is significantly lower than that on the single components, indicating that the heterojunction interface greatly promotes the Volmer step ($H_2O + e^- \rightarrow H + OH^-$). Under acidic conditions (Fig. 4(i)), the Gibbs free energy of H adsorption (ΔG_H) on the heterojunction model is −0.046 eV, which is very close to the ideal value of 0 eV and far superior to that of pure RuP_2 and Ni_2P. This suggests that it possesses a near-optimal hydrogen adsorption/desorption capability [59].

4 Conclusions

This work presents a synergistic heterojunction-and-hollow-confinement design, yielding RuP_2-Ni_2P nanoparticles embedded in N,P-codoped carbon spheres. The intimate RuP_2-Ni_2P interface optimizes the electronic structure for near-ideal hydrogen adsorption, while the embedded hollow architecture maximizes active site exposure and ensures exceptional stability. Consequently, the catalyst delivers superior HER activity with record-low overpotentials and robust durability across wide pH, alongside high noble-metal mass activity. This study offers an effective strategy for designing high-performance, durable HER electrocatalysts.

Electronic Supplementary Material: Supplementary material (additional characterization spectra, electrochemical test data, elemental analysis results, and DFT calculation details, which provide further support for the conclusions presented in the main text) is available in the online version of this article at https://doi.org/10.26599/NR.2026.94908616.

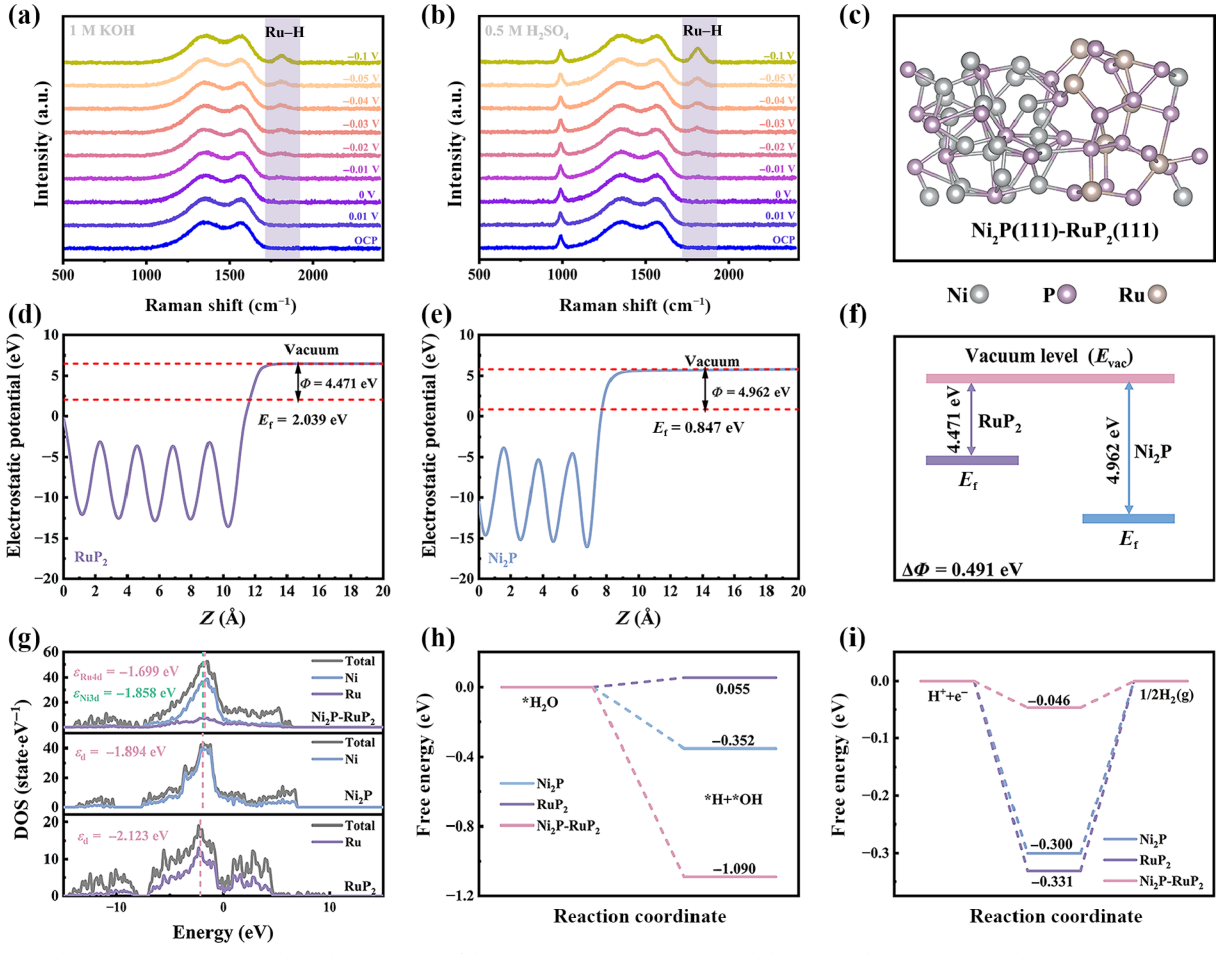

Figure 4 Mechanistic insights into the enhanced HER activity of the RuP_2-Ni_2P heterostructure revealed by *operando* spectroscopy and DFT calculations. *In situ* Raman spectra of RuP_2-Ni_2P/NPC recorded at various applied potentials in (a) 1 M KOH and (b) 0.5 M H_2SO_4. (c) Optimized structural model of the Ni_2P (111)-RuP_2 (111) heterojunction interface. Calculated work functions (Φ) of (d) RuP_2 (111) and (e) Ni_2P (111), and (f) their difference $\Delta\Phi$. (g) Projected density of states (PDOS) for the Ni_2P-RuP_2 heterostructure and the isolated Ni_2P and RuP_2 components; the dashed lines indicate the d-band centers. Gibbs free energy diagrams for HER on Ni_2P-RuP_2 heterostructure and reference surfaces under (h) alkaline and (i) acidic conditions.

Data availability

All data needed to support the conclusions in the paper are presented in the manuscript and the Electronic Supplementary Material. Additional data related to this paper may be requested from the corresponding author upon request.

Acknowledgements

This work was financially supported by the National Natural Science Foundation of China (No. 52271184), General Scientific Research Project of the Department of Education of Zhejiang Province (No. Y202557367), High-level Talents Special Support Program of Taizhou, Science and Technology Plan Project of Taizhou (No. 25gya12), and High-level Talents Special Support Program of Taizhou.

Declaration of competing interest

All the contributing authors report no conflict of interests in this work.

Author contribution statement

D. Y.: Investigation, data curation. C. C.: Investigation, data curation. H. H. Z.: Project administration, writing – review & editing. J. J. G.: Project administration, resources. L. L. Z.: Funding acquisition, resources, writing – review & editing. L. G.: Supervision. S. J. S: Funding acquisition, supervision, writing – original draft, writing – review & editing. W. W. Z.: Supervision, project administration, writing – review & editing, resources. All the authors have approved the final manuscript.

Use of AI statement

None.

References

[1] Sha, Q. H.; Wang, S. Y.; Yan, L.; Feng, Y. S.; Zhang, Z.; Li, S. H.; Guo, X. L.; Li, T. S.; Li, H.; Zhuang, Z. B. et al. 10,000-h-stable intermittent alkaline seawater electrolysis. *Nature* **2025**, *639*, 360–367.

[2] Li, Q. G.; Zhang, H. H.; Yang, D.; Gong, J. J.; Zhang, L. L.; Gu, L.; Chen, S. C.; Shen, S. J.; Zhong, W. W. Cationic defect-enabled charge transfer in rhodium clusters via Rh–O bonding for enhanced alkaline hydrogen evolution. *Nano Res.* **2025**, *18*, 94907391.

[3] Yan, Z. X.; Gong, J. J.; Sun, H. L.; Jin, T. C.; Yang, D.; Gu, L.; Zhang, L. L.; Shen, S. J.; Zhong, W. W. Heterojunction-doping synergy in strontium palladium-ruthenium oxide catalysts for efficient oxygen evolution. *Nano Res.* **2026**, *19*, 94908006.

[4] Zou, R. Q.; Liu, S. B.; Su, J.; Ding, W. H.; Wang, Y. J.; Yan, F.; Guo, P.; Zhou, J. C.; Zhang, Y. Z.; Li, X. H. Nickel carrier transfer bridge for improved photocatalytic water splitting of Zn_2GeO_4. *Trans. Mater. Res.* **2025**, *1*, 100006.

[5] Feng, Y. M.; Xie, Y. H.; Yu, Y. J.; Chen, Y. Z.; Liu, Q. T.; Bao, H. F.; Luo, F.; Pan, S. Y.; Yang, Z. H. Electronic metal-support interaction induces hydrogen spillover and platinum utilization in hydrogen evolution reaction. *Angew. Chem., Int. Ed.* **2025**, *64*, e202413417.

[6] Shen, S. J.; Li, Q. G.; Zhang, H. H.; Yang, D.; Gong, J. J.; Gu, L.; Gao, T.; Zhong, W. W. Negative-valent platinum stabilized by Pt–Ni electron bridges on oxygen-deficient NiFe-LDH for enhanced electrocatalytic hydrogen evolution. *Adv. Mater.* **2025**, *37*, 2500595.

[7] Shen, S. J.; Wang, Z. P.; Lin, Z. P.; Song, K.; Zhang, Q. H.; Meng, F. Q.; Gu, L.; Zhong, W. W. Crystalline-amorphous interfaces coupling of $CoSe_2$/CoP with optimized d-band center and boosted electrocatalytic hydrogen evolution. *Adv. Mater.* **2022**, *34*, 2110631.

[8] Wang, X. Q.; Zhang, J. T.; Wang, Z. P.; Lin, Z. P.; Shen, S. J.; Zhong, W. W. Fabricating Ru single atoms and clusters on CoP for boosted hydrogen evolution reaction. *Chin. J. Struct. Chem.* **2023**, *42*, 100035.

[9] Yue, H. Y.; Guo, Z. N.; Guo, W. J.; Yao, R. N.; Zhen, S.; Ma, Q. S.; Chen, M.; Lin, J. W.; Yuan, W. X. Lattice distortion in high-entropy transition metal diselenide for augmented hydrogen evolution. *Adv. Mater.* **2026**, *38*, e22787.

[10] Yue, H. Y.; Guo, Z. N.; Zhou, Z. W.; Zhang, X. M.; Guo, W. J.; Zhen, S.; Wang, P.; Wang, K.; Yuan, W. X. S–S bond strategy at sulfide heterointerface: Reversing charge transfer and constructing hydrogen spillover for boosted hydrogen evolution. *Angew. Chem., Int. Ed.* **2024**, *63*, e202409465.

[11] Li, Y. Q.; Liu, X.; Xu, J. L.; Chen, S. R. Ruthenium-based electrocatalysts for hydrogen evolution reaction: From nanoparticles to single atoms. *Small* **2024**, *20*, 2402846.

[12] Luo, J. H.; Wang, J.; Guo, Y.; Zhu, J. W.; Jin, H. H.; Zhang, Z. W.; Zhang, D. J.; Niu, Y. S.; Hou, S. G.; Du, J. M. et al. Metal-organic frameworks derived RuP_2 with yolk-shell structure and efficient performance for hydrogen evolution reaction in both acidic and alkaline media. *Appl. Catal. B: Environ.* **2022**, *305*, 121043.

[13] Qin, S. H.; Banerjee, S.; Sensoy, M. G.; Rappe, A. M. Unveiling the electrocatalytic hydrogen evolution reaction pathway on RuP_2 through *ab initio* grand canonical Monte Carlo. *ACS Catal.* **2024**, *14*, 17253–17262.

[14] Li, Y. P.; Zhang, J. H.; Liu, Y.; Qian, Q. Z.; Li, Z. Y.; Zhu, Y.; Zhang, G. Q. Partially exposed RuP_2 surface in hybrid structure endows its bifunctionality for hydrazine oxidation and hydrogen evolution catalysis. *Sci. Adv.* **2020**, *6*, eabb4197.

[15] Zhao, Y.; Zhang, X. Y.; Gao, Y. X.; Chen, Z.; Li, Z. J.; Ma, T. Y.; Wu, Z. X.; Wang, L.; Feng, S. H. Heterostructure of RuO_2–RuP_2/Ru derived from HMT-based coordination polymers as superior pH-universal electrocatalyst for hydrogen evolution reaction. *Small* **2022**, *18*, 2105168.

[16] Zhang, S. T.; Liu, M. Y.; Liu, J. N.; Xu, Z. X.; Liu, Q. X.; Wang, R. H.; Meng, H. Y.; Jiang, B. J. Asymmetric electronic structure at the interface Ni–P–Ru bridge inducing dual active sites for electrocatalytic urea-assisted water splitting. *Chem. Eng. J.* **2025**, *520*, 166029.

[17] Zhou, F.; Sa, R.; Zhang, X.; Zhang, S.; Wen, Z. H.; Wang, R. H. Robust ruthenium diphosphide nanoparticles for pH-universal hydrogen evolution reaction with platinum-like activity. *Appl. Catal. B: Environ.* **2020**, *274*, 119092.

[18] Zhou, Y. N.; Wang, F. L.; Nan, J.; Dong, B.; Zhao, H. Y.; Wang, F. G.; Yu, N.; Luan, R. N.; Liu, D. P.; Chai, Y. M. High-density ultrafine RuP_2 with strong catalyst-support interaction driven by dual-ligand and tungsten-oxygen sites for hydrogen evolution at 1 $A \cdot cm^{-2}$. *Appl. Catal. B: Environ.* **2022**, *304*, 120917.

[19] Wu, Z. X.; Li, Q. C.; Xu, G. R.; Jin, W.; Xiao, W. P.; Li, Z. J.; Ma, T. Y.; Feng, S. H.; Wang, L. Microwave phosphine-plasma-assisted ultrafast synthesis of halogen-doped Ru/RuP_2 with surface intermediate adsorption modulation for efficient alkaline hydrogen evolution reaction. *Adv. Mater.* **2024**, *36*, 2311018.

[20] Cao, L. M.; Yu, L. H.; Huang, H. B.; Gao, C. J.; Huang, X.; Zhang, X. F.; Zhang, X. H.; Du, Z. Y.; He, C. T. A molecular engineered strategy to remolding architecture of RuP_2 nanoclusters for sustainable hydrogen evolution. *Adv. Funct. Mater.* **2024**, *34*, 2411111.

[21] Pu, Z. H.; Amiinu, I. S.; Kou, Z. K.; Li, W. Q.; Mu, S. C. RuP_2-based catalysts with platinum-like activity and higher durability for the hydrogen evolution reaction at all pH values. *Angew. Chem., Int. Ed.* **2017**, *56*, 11559–11564.

[22] Tong, K. C.; Xu, L. L.; Yao, H. X.; Wang, X. K.; Zhang, C. H.; Yang,

F.; Chu, L.; Lee, J.; Jiang, H. Q.; Huang, M. H. Hydrogen spillover bridged dual nano-islands triggered by built-in electric field for efficient and robust alkaline hydrogen evolution at ampere-level current density. *Nano Res.* **2024**, *17*, 5050–5060.

[23] Liu, S. S.; Zhu, J. Y.; Xu, X. F.; Li, J. S. Three-dimensional graphene-supported CoP–RuP_2 with artificial heterointerfaces for an enhanced universal-pH hydrogen evolution reaction. *Cryst. Growth Des.* **2022**, *22*, 5607–5615.

[24] Wang, J.; Zhou, Y. S.; Ji, X.; Wang, Z. Z.; Fang, Z. F.; Lu, B.; Guo, J. J.; Wei, Z. Z. Coupling highly reactive RuP_2 with amorphous WP for boosting alkaline hydrogen evolution. *J. Alloys Compd.* **2024**, *1008*, 176695.

[25] Chen, L. Z.; Fang, Y.; Pang, M. X.; Sun, R. X.; Xu, L.; Zhou, Q. X.; Tang, Y. W. Interfacial engineering of core/satellite-structured RuP/RuP_2 heterojunctions for enhancing pH-universal hydrogen evolution reaction. *Chin. J. Struct. Chem.* **2025**, *44*, 100461.

[26] Jiang, Y. N.; Du, L. L.; Sun, W. X.; Zhang, Q.; Su, Y. W.; Sun, M. L.; Yin, G. C. Constructing tungsten doping RuP_2@carbon dots for enhanced hydrogen evolution reaction in acidic and alkaline media. *Int. J. Hydrogen Energy* **2024**, *51*, 725–732.

[27] Yu, J.; Wu, X. H.; Zhang, H. J.; Ni, M.; Zhou, W.; Shao, Z. P. Core effect on the performance of N/P codoped carbon encapsulating noble-metal phosphide nanostructures for hydrogen evolution reaction. *ACS Appl. Energy Mater.* **2019**, *2*, 2645–2653.

[28] Zhang, H.; Liao, J. J.; Chen, L.; Chen, X. Y.; Yu, Z. P.; Yin, H.; Zhang, J.; Hou, Z. H.; Huang, J. L. Low-amount RuP_2 nanocluster anchored on P, N-codoped carbon with optimized H and H_2O adsorption boost hydrogen evolution in anion-exchange membrane water electrolyzer. *Rare Met.* **2025**, *44*, 6268–6278.

[29] Kirubasankar, B.; Kwon, J.; Hong, S.; Won, Y. S.; Choi, S. H.; Lee, J.; Kim, J. W.; Kim, K. K.; Kim, S. M. A robust and highly active bimetallic phosphide/oxide heterostructure electrocatalyst for efficient industrial-scale hydrogen production. *Nano Energy* **2024**, *128*, 109805.

[30] Sun, Y.; Li, H. B.; Zeng, S. Y.; Li, R.; Yao, Q. X.; Chen, H. Y.; Wang, Y. H.; Qu, K. G.; Meng, L. J. Confined RuP_2 nanoparticles in N,P,S-tridoped carbon as superior electrocatalyst for pH-wide hydrogen evolution. *Chem. Asian, J.* **2025**, *20*, e00511.

[31] Kresse, G.; Furthmüller, J. Efficient iterative schemes for *ab initio* total-energy calculations using a plane-wave basis set. *Phys. Rev. B* **1996**, *54*, 11169–11186.

[32] Parkinson, G. S.; Novotny, Z.; Argentero, G.; Schmid, M.; Pavelec, J.; Kosak, R.; Blaha, P.; Diebold, U. Carbon monoxide-induced adatom sintering in a Pd–Fe_3O_4 model catalyst. *Nat. Mater.* **2013**, *12*, 724–728.

[33] Kresse, G.; Joubert, D. From ultrasoft pseudopotentials to the projector augmented-wave method. *Phys. Rev. B* **1999**, *59*, 1758–1775.

[34] Grimme, S.; Ehrlich, S.; Goerigk, L. Effect of the damping function in dispersion corrected density functional theory. *J. Comput. Chem.* **2011**, *32*, 1456–1465.

[35] Sun, H.; Li, Y. Z.; Gao, L. Y.; Chang, M. Y.; Jin, X. R.; Li, B. Y.; Xu, Q. Z.; Liu, W.; Zhou, M. Y.; Sun, X. M. High throughput screening of single atomic catalysts with optimized local structures for the electrochemical oxygen reduction by machine learning. *J. Energy Chem.* **2023**, *81*, 349–357.

[36] Liu, Y.; Cheng, L. R.; Zhou, S. Q.; Niu, C. G.; Isimjan, T. T.; Yang, X. L. Built-in electric field-driven electron transfer behavior at Ru–RuP_2 heterointerface fosters efficient and CO-resilient alkaline hydrogen oxidation. *Appl. Catal. B: Environ. Energy* **2025**, *362*, 124709.

[37] Tian, X.; Wang, Z. P.; Cai, Z. H.; Ma, X.; Wang, S. RuP_2/CoP heterointerfaces: A universal pH-independent catalyst for electrolytic hydrogen generation. *Int. J. Hydrogen Energy* **2025**, *124*, 1–7.

[38] Song, H. Q.; Cheng, Y. J.; Li, B. J.; Fan, Y. P.; Liu, B. Z.; Tang, Z. Y.; Lu, S. Y. Carbon dots and RuP_2 nanohybrid as an efficient bifunctional catalyst for electrochemical hydrogen evolution reaction and hydrolysis of ammonia borane. *ACS Sustainable Chem. Eng.* **2020**, *8*, 3995–4002.

[39] Liu, T. T.; Chen, C.; Pu, Z. H.; Zhang, X. F.; Huang, Q. F.; Al-Enizi, A. M.; Nafady, A.; Chen, Z. S.; Sun, S. H.; Zhang, G. X. Joule heating to grain-boundary-rich RuP_2 for efficient electrocatalytic hydrogen evolution in a wide pH range. *Energy Mater.* **2025**, *5*, 500058.

[40] Shen, S. Y.; Zhang, Q.; Guo, W. J.; Jiao, G. J.; Wang, Y. W.; Wang, H.; Shao, K.; Wang, Z. J.; Li, C. C.; Peng, X. Y. et al. RuP_2 nanoparticles decorated on natural cellulose nanofibrils-derived N, P codoped carbon matrix for hydrogen evolution at dual pH and seawater. *ACS Appl. Nano Mater.* **2025**, *8*, 11800–11810.

[41] Li, P.; Li, W. Q.; Huang, Y. Q.; Li, J. X.; Huang, Q. H.; Zhao, S. E.; Tian, S. H. Encapsulated RuP_2–RuS_2 nanoheterostructure with regulated interfacial charge redistribution for synergistically boosting hydrogen evolution electrocatalysis. *Nanoscale* **2022**, *14*, 6258–6267.

[42] Wu, W. J.; Guo, W. X.; Liu, Z. Y.; Zhang, C. X.; Li, A. B.; Su, C. H.; Wang, C. X. Interface-engineered RuP_2/$Mn_2P_2O_7$ heterojunction on N/P co-doped carbon for high-performance alkaline hydrogen evolution. *Materials* **2025**, *18*, 3065.

[43] Chang, Q. B.; Ma, J. W.; Zhu, Y. Z.; Li, Z.; Xu, D. Y.; Duan, X. Z.; Peng, W. C.; Li, Y.; Zhang, G. L.; Zhang, F. B. et al. Controllable synthesis of ruthenium phosphides (RuP and RuP_2) for pH-universal hydrogen evolution reaction. *ACS Sustainable Chem. Eng.* **2018**, *6*, 6388–6394.

[44] Li, J. S.; Huang, M. J.; Zhou, Y. W.; Chen, X. N.; Yang, S.; Zhu, J. Y.; Liu, G. D.; Ma, L. J.; Cai, S. H.; Han, J. Y. RuP_2-based hybrids derived from MOFs: Highly efficient pH-universal electrocatalysts for the hydrogen evolution reaction. *J. Mater. Chem. A* **2021**, *9*, 12276–12282.

[45] Wang, Y. H.; Li, R. Q.; Li, H. B.; Huang, H. L.; Guo, Z. J.; Chen, H. Y.; Zheng, Y.; Qu, K. G. Controlled synthesis of ultrasmall RuP_2 particles on N,P-codoped carbon as superior pH-wide electrocatalyst for hydrogen evolution. *Rare Met.* **2021**, *40*, 1040–1047.

[46] Gao, Y. X.; Chen, Z.; Zhao, Y.; Yu, W. L.; Jiang, X. L.; He, M. S.; Li, Z. J.; Ma, T. Y.; Wu, Z. X.; Wang, L. Facile synthesis of MoP–Ru_2P on porous N, P co-doped carbon for efficiently electrocatalytic hydrogen evolution reaction in full pH range. *App. Catal. B: Environ.* **2022**, *303*, 120879.

[47] Zhao, J.; Chen, Z. H.; Sun, L. L.; Yan, J. P.; Xue, P. Y.; Xue, L. R.; Liu, J. Relatively low crystalline heterojunction Ru–RuP_2/WC for hydrogen evolution reaction in proton exchange membrane water electrolyzer. *ChemCatChem* **2025**, *17*, e01072.

[48] Luo, L. L.; Liu, C. H.; Li, Z.; Zhang, L. L.; Xie, W. T.; Zhang, T. T.; Chen, Z. D. Anchoring ultrafine molybdenum phosphide on hierarchical three-dimensional CNTs/rGO framework as efficient electrocatalysts for hydrogen evolution. *J. Mater. Sci.: Mater. Electron.* **2022**, *33*, 3175–3185.

[49] Jiang, H.; Zhang, H.; Chen, D. M.; Lin, X.; Zuo, X. Q.; Yang, Q.; Tang, H. B.; Li, G. Heterostructured ruthenium phosphide (RuP)/Ru was obtained by SiO_2 template method for alkaline and acidic hydrogen evolution reactions. *Mater. Lett.* **2026**, *403*, 139434.

[50] Liu, Y.; Li, X.; Zhang, Q. H.; Li, W. D.; Xie, Y.; Liu, H. Y.; Shang, L.; Liu, Z. Y.; Chen, Z. M.; Gu, L. et al. A general route to prepare low-ruthenium-content bimetallic electrocatalysts for pH-universal hydrogen evolution reaction by using carbon quantum dots. *Angew. Chem., Int. Ed.* **2020**, *59*, 1718–1726.

[51] Li, Y. P.; Wang, W. T.; Cheng, M. Y.; Feng, Y. F.; Han, X.; Qian, Q. Z.; Zhu, Y.; Zhang, G. Q. Arming Ru with oxygen-vacancy-enriched RuO_2 sub-nanometer skin activates superior bifunctionality for pH-universal overall water splitting. *Adv. Mater.* **2023**, *35*, 2206351.

[52] Sun, F. Y.; Ju, Y. W.; Zhao, Y. X.; Yue, C. L.; Liu, N.; Hao, H. Y.; Xu, Y. Y.; Wang, F.; Wang, J. Q.; Lu, Y. K. Hierarchical confinement-

electronic modulation strategy: Ru assisted ultrafine α-MoC in porous carbon to optimize reaction kinetics for hydrogen evolution reaction. *App. Catal. B: Environ. Energy* **2026**, *382*, 125946.

[53] Jiao, J. Q.; Zhang, N. N.; Zhang, C.; Sun, N.; Pan, Y.; Chen, C.; Li, J.; Tan, M. J.; Cui, R. X.; Shi, Z. L. et al. Doping ruthenium into metal matrix for promoted pH-universal hydrogen evolution. *Adv. Sci.* **2022**, *9*, 2200010.

[54] Yang, Y. Q.; Pang, D. W.; Wang, C. J.; Fu, Z. H.; Liu, N. Y.; Liu, J. J.; Wu, H. J.; Jia, B. B.; Guo, Z. L.; Fan, X. Y. et al. Vacancy and dopant co‐constructed active microregion in Ru–MoO_{3-x}/Mo_2AlB_2 for enhanced acidic hydrogen evolution. *Angew. Chem., Int. Ed.* **2025**, *64*, e202504084.

[55] Qiu, T. J.; Liang, Z. B.; Guo, W. H.; Gao, S.; Qu, C.; Tabassum, H.; Zhang, H.; Zhu, B. J.; Zou, R. Q.; Shao-Horn, Y. Highly exposed ruthenium-based electrocatalysts from bimetallic metal-organic frameworks for overall water splitting. *Nano Energy* **2019**, *58*, 1–10.

[56] Wang, X. W.; Yu, L.; Lu, Z. H.; Liu, C. X.; Zhao, B.; Lv, C. M.; Xie, Y.; Kan, W. A "Two-Pronged" strategy via tungsten doping and heterostructure to boost hydrogen evolution reaction in pH-universal media. *ACS Sustainable Chem. Eng.* **2025**, *13*, 5633–5644.

[57] Zhao, H.; Ni, B. X.; Pan, Y. Y.; Li, Y. Z.; Li, J.; Wang, G. L.; Zou, Z. Q.; Jiang, K.; Cheng, Q. Q.; Zu, L. H. et al. Key role of bridge adsorbed hydrogen intermediate on Pt–Ru pair for efficient acidic hydrogen production. *Adv. Mater.* **2025**, *37*, 2503221.

[58] Jiang, H.; Yang, N.; Yang, X. D.; Shen, H. C.; Zhang, L. F.; Zhou, S. S.; Li, Z. C.; Xiao, X. M.; Sun, Y. L.; Tantai, X. et al. Spatially coupled Ni_2P/CoP-8 heterostructures with superwetting interfaces for high current density overall water splitting. *J. Colloid Interface Sci.* **2026**, *706*, 139565.

[59] Wu, G.; Han, X.; Cai, J. Y.; Yin, P. Q.; Cui, P. X.; Zheng, X. S.; Li, H.; Chen, C.; Wang, G. M.; Hong, X. In-plane strain engineering in ultrathin noble metal nanosheets boosts the intrinsic electrocatalytic hydrogen evolution activity. *Nat. Commun.* **2022**, *13*, 4200.